P. Niederdrenk
Research Scientist.

H. Sobieczky
Research Scientist.

Institute for Theoretical Fluid Mechanics,
DFVLR,
Göttingen, Federal Republic of Germany

G. S. Dulikravich
Associate Professor,
Department of Aerospace Engineering,
Pennsylvania State University,
University Park, PA
Mem. ASME

Supercritical Cascade Flow Analysis With Shock-Boundary Layer Interaction and Shock-Free Redesign

This paper describes improvements made in a user-oriented analysis code for steady two-dimensional transonic flows in turbomachinery cascades. The full potential equation is solved by a finite area technique, using a C-type grid and an analytical wake model. Solution adaptive grid clustering refines the inviscid computationally captured shock. The boundary layer is computed by an integral method except in the shock region, where the analytical interaction model of Bohning and Zierep smoothes out the pressure distribution on the airfoil surface. The code is applied in its analysis and design modes to an experimentally tested cascade of airfoils.

Introduction

At high subsonic inlet Mach numbers, transonic cascade flow is usually characterized by local supersonic regions. In order to avoid strong shock losses and minimize viscous losses the blades should be shaped to provide supercritical flow with nearly isentropic recompression at the design point. The general aim is to obtain larger ranges of operating inlet Mach number and incidence angles while keeping the losses acceptably low at the same time. During off-design performance these losses are mainly due to shock waves terminating the supersonic regions and interacting with the boundary layer. Changes in the profile thickness of the order of the boundary layer displacement thickness, particularly in the supersonic region, may shift a shockless cascade flow into a shocked flow.

Thus, careful blade design requires an accurate prediction method including viscous/inviscid interaction effects. Although solving the Navier–Stokes equations in the whole flow field would certainly be the most complete model, we prefer the efficient approach of iterating solutions in different parts of the flowfield to a composite solution until convergence is achieved. At the high Reynolds numbers of practical interest the shear layers are thin and viscous effects can be attributed to an overall viscous/inviscid interaction between boundary layer, wake, and external inviscid flow. The generally weak global interaction may be significantly augmented at transonic speeds by strong local interactions between the shock wave and the turbulent boundary layer as well as between the external inviscid flow and the highly curved streamlines in the near-wake region at the trailing edge. Here we have to account for large normal pressure gradients, which cause the usual boundary layer assumptions to break down.

To describe the local interaction of a normal shock with the turbulent boundary layer we apply the analytical model of Bohning and Zierep [1, 2]. This model yields nonasymptotic small perturbation solutions of the Navier–Stokes equations for a thin viscous sublayer adjacent to the wall and an inviscid shear layer for the main part of the boundary layer. We embedded these solutions in an integral boundary layer method [3] and iteratively coupled them using a displacement thickness concept to an outer potential flow solver [4]. The wake is presently incorporated by a simple analytical model.

Although different in its individual calculation procedures and their coupling, this process may be compared to the "Grumfoil" code developed by Melnik et al. [5]. This work was recently extended by Inger's shock-boundary layer interaction treatment [6]. While the Grumfoil algorithm takes better account of strongly curved near-wake flow, due to the implementation of the results of Melnik and Chow [7], our code is developed for cascade flows and incorporates an extra design option. As outlined already for inviscid cascade flow in [8], the fictitious gas concept is applied to provide modifications of the blade contour necessary to allow for shock-free flow at supercritical operating conditions. It is that flexibility of the code which provides the practicing engineer with a tool to analyze a given cascade's performance and redesign it in order to improve its efficiency.

Computational Grid Generation

Using a finite area technique for the inviscid flow computation the grid does not have to be strictly orthogonal. Therefore, we generate the grid very economically by combining two analytically defined conformal mappings followed by separate coordinate shearing and stretching transformations [10]. This significantly speeds up the overall computation since in our viscous/inviscid coupling procedure the grid has

Contributed by the Gas Turbine Division for publication in the JOURNAL OF TURBOMACHINERY. Manuscript received by the Gas Turbine Division November 7, 1984.

to be repeatedly created for each global iteration cycle not only due to the varying displacement thickness but also due to the local grid reclustering at the intermediate shock positions.

When a shock capturing technique is employed, the shock discontinuity is approximated by strong gradients of the flow variables due to artificial viscosity added in the supersonic region. The distance over which the jump is smeared is generally of the same order of magnitude as the shock–boundary layer interaction zone, especially at the high Reynolds numbers of interest. Thus the localization of the smearing yields another reason for smooth grid refinement at the shock.

Our grid-generating procedure requires just the position of the shock along the chord and the distance between two surface points where clustering additional to the leading and trailing edge regions is desired. A detail of the grid around a compressor blade shown in Fig. 1 is depicted in Fig. 2, showing that the grid is clustered on the upper surface at $x/c = 0.33$.

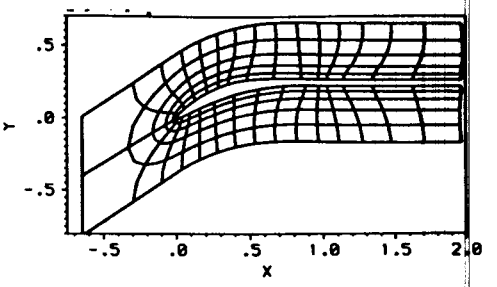

Fig. 1 C-type grid for a staggered compressor cascade with wake included

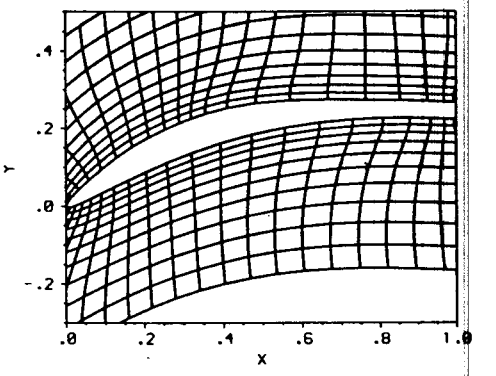

Fig. 2 Local grid clustering at x = 0/0.33/1

Inviscid Flow Analysis

As already mentioned, we use the full potential equation

$$(1-\Phi_x^2/a^2)\Phi_{xx}+2(\Phi_x\Phi_y/a^2)\Phi_{xy}+(1-\Phi_y^2/a^2)\Phi_{yy}=0 \qquad (1)$$

This may be regarded as the continuity equation for an inviscid isentropic steady flow of an ideal gas. We numerically solve its divergence-free form to treat discontinuous solutions properly

$$(\rho u)_x+(\rho v)_y=0 \qquad (2)$$

In addition to conservation of mass and energy, we impose constant entropy as a third condition. Thus the momentum equation cannot be satisfied across isentropic shock waves, which means that the preshock Mach number should not be substantially greater than 1.3 to limit the deviations from the correct Rankine–Hugoniot jumps.

As described in earlier papers [4, 8], the finite area technique is used to solve equation (2) subject to uniform flow conditions at the upstream and downstream flow field boundaries.

Treatment of Viscous Layers

For the computation of the boundary layer we employ Rotta's integral dissipation method [3]. It solves simultaneously von Karman's momentum equation and the mechanical energy equation, utilizing additional empirical relations for the shape factors, the skin friction coefficient, and the dissipation coefficient.

When we march under the shock, normal pressure gradients cause a perturbation of the boundary layer. Neglecting the dependence of the undisturbed flow in the streamwise direction within the small interaction region, Bohning and Zierep derived linearized perturbation equations from the continuity, Navier–Stokes, and energy equations. As their model has been already described in the literature [1, 2], only a brief look at some of its essential features will be given here. Following Lighthill's concept the turbulent boundary layer is divided into two compressible layers (see Fig. 3). In the outer layer friction is considered only due to the incoming undisturbed velocity profile while the perturbations lend themselves to an essentially inviscid boundary value problem. Approximating the undisturbed velocity and Mach number profiles by power law functions, the resulting second-order differential equation is solved analytically containing the thickness of the inner wall layer as a yet unknown parameter. Within the inner layer, which turns out to be of the order of 1 percent of the boundary layer thickness, the Mach number typically decreases from

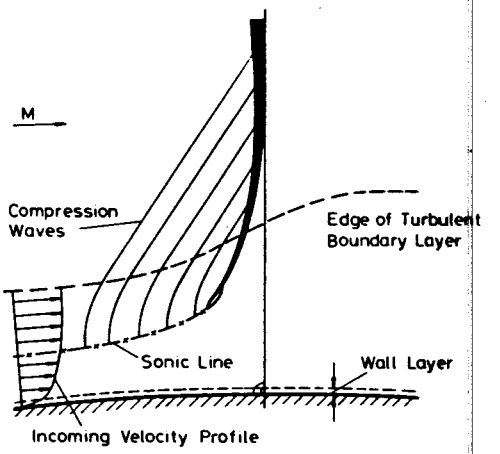

Fig. 3 Sketch of shock-boundary layer interaction model

Nomenclature

a = speed of sound
c = cascade airfoil maximum chord length
C_p = pressure coefficient
g = gap distance between leading edges of two neighboring airfoils in the cascade
H_{32} = boundary layer shape factor $= \delta_3/\delta_2$
M = Mach number
Re = Reynolds number
w = velocity
β = flow angle measured from the circumferential direction
β_s = stagger angle
δ_1 = boundary layer displacement thickness
δ_2 = boundary layer momentum thickness
δ_3 = boundary layer energy thickness
ρ = fluid density
Φ = velocity potential
ω = relaxation coefficient
Ω = axial velocity density relation $= (\rho_2 w_2 \sin \beta_2)/(\rho_1 w_1 \sin \beta_1)$

about 0.5 to zero at the wall. A closed-form solution of the linearized compressible boundary layer equations yields on one hand the thickness of this layer and on the other hand – in combination with a suitable law of the wall for the undisturbed profile – the wall shear stress.

As the basic incoming boundary layer quantities are frozen over the streamwise extent of the interaction region, the variations of the perturbations have to vanish at $x \to \pm\infty$. Thus the solution must exhibit an asymptotic behavior. Actually, because of its exponential decay, the wall pressure perturbation, for example, tends to zero within a few boundary layer thicknesses (typically within 2 percent of chord). Having replaced the assumed analytical structure of the inviscid pressure distribution in the original version by the numerical calculation of the external flow field, we attach the perturbation solution to the ordinary boundary layer calculation at such streamwise locations that the latter will not be subjected to the sharp pressure rise across the shock. These locations, although depending on Reynolds number and grid refinement, are usually given by the extent of potential shock smearing due to artificial viscosity, as mentioned before. At the end of the interaction zone we have all possible integral boundary layer quantities at our disposal. Solving for the displacement thickness we evaluate δ_1 and the shape factor H_{32} at the end of the interaction and submit these quantities to reinitiate the boundary layer code after the shock.

At present we treat the wake as a viscous displacement model of constant thickness given by the sum of the trailing edge and boundary layer displacement thicknesses. Instead of fulfilling the Kutta condition the wake is adjusted to the solution with regard to pressure equality on its upper and lower surfaces by iterating on its curvature only. Within the overall iteration process between inviscid and viscous parts of the flow field this concept can easily be extended to a more appropriate wake treatment including other parameters, e.g., variable wake displacement thickness and/or variable exit flow angle [11].

Viscous-Inviscid Coupling

In transonic flow over an airfoil we are concerned with regions of weak and strong viscous/inviscid interactions. The weak interaction arises from boundary layer displacement and global wake curvature effects. Here we have no convergence problems following the direct global iteration approach: Prescribe the inviscid pressure distribution as a boundary condition for the boundary layer calculation and use the resulting displacement thickness to correct the airfoil contour for blockage effects.

When adverse local pressure gradients cause stronger interaction the direct iteration approach becomes unstable. Damping of the instability is usually provided by underrelaxing the displacement thickness. At the location of very strong pressure gradients due to shock waves or highly curved streamlines in the near wake this procedure would require vanishing relaxation coefficients. At the same time the ordinary boundary layer equations no longer represent the adequate model.

Having partially accounted for this problem by employing the Bohning–Zierep interaction theory at the shock, we still encounter stability problems on the suction surface near the trailing edge. At present we circumvent this shortcoming by linearly extrapolating the pressure distribution to be submitted to the boundary layer code from about 97 percent of the chord up to the trailing edge.

In the potential flow calculation we use a grid-refinement sequence consisting of four consecutively refined grids. In order to save time we could use the ordinary boundary layer integral code on a coarse grid during the first iterations even in the shock region, if the pressure gradient were sufficiently smeared. Hence we introduce a simple analytical function to smear out the pressure rise widely across the inviscid shock during the first two global viscous/inviscid iterations. In fact the adverse velocity gradients predicted by the full potential code in regions of strong interaction are much greater than they will be in the final converged state. So, in anticipation of the qualitative form of the final result, we are able to increase the convergence rate of the global iterative procedure while assuring its stability. Thus the boundary layer code does not signalize separation due to shock-induced strong pressure gradients during the early stage of the iterative process. In order to get a smooth transition to the actually calculated inviscid pressure distribution, which is submitted to the viscous part of the employed local analysis on the third and fourth grid, we also underrelax the pressure. Applying this simple procedure the shock moves only a few grid points during the iterations and convergence is generally obtained after five to seven global cycles.

Results

In order to minimize effects of the trailing edge, where our treatment of the viscous flow still needs substantial improvements, we choose as a first example the symmetric NACA 0012 profile at zero incidence and a free-stream Mach number of 0.77. Starting the iterative cycle on a coarse grid with only 20 grid points along the suction surface, the resulting pressure distribution of the inviscid flow field calculation shown in Fig. 4(*a*) is analytically smeared out over the shock region. Thus the ordinary boundary layer method employed over the whole profile up to the third global iteration does not immediately signal turbulent separation. The resulting displacement thickness (indicated by crosses in Fig. 4*a*) is underrelaxed (solid line in Fig. 4*b*) before it is added to the profile contour. At the third and fourth steps (Fig. 4*c*, *d*) the grid size is halved each time. Near the shock the grid is clustered just to such an extent that unphysical preshock peaks in Mach number are avoided. On the finest grid (Fig. 4*d*, *e*, *f*, *g*) the interaction theory is employed in the shock region and the whole viscous calculation subjected to an underrelaxed pressure distribution. The main effect of relaxing the pressure is again to smear out the streamwise pressure gradient while the shock is still moving during the iteration and thus to stabilize the process of finding stationary positions of the shock and the accompanying boundary layer thickening.

Finally, when global convergence is achieved, the boundary layer is subjected to the correct pressure distribution, its jump across the shock being felt as sharp as provided by the inviscid flowfield calculation in connection with local grid clustering. Due to inviscid potential shock smearing the continuous wall pressure distribution at this high Reynolds number practically coincides with the pressure at the outer edge of the boundary layer. For reasons of clarity only the latter is shown in the figures. Since our finite area inviscid flow analysis code can handle the bumps in displacement thickness produced by the interaction theory, no additional smoothing is needed. Thus the very small change in displacement thickness occurring at transition from laminar to turbulent boundary layer (x/c = 0.07) is evident in the pressure distribution (Fig. 4*g*).

When the inviscid flow begins to react with the steeper increase in displacement thickness (Fig. 4*e*, *f*, *g*) the previously observed inviscid postshock expansion at the shock root gradually vanishes. For the pre- and postshock Mach numbers taken from the sample calculation the shock polar diagram (Fig. 5) leads to a deflection angle of 3.85 deg. This value is embedded within the limits given for sonic conditions and maximum deflection at an attached shock, respectively: a feature which is also confirmed by experimental observation.

Changing over to a typical user-oriented problem we analyze an actual supercritical blade section developed and

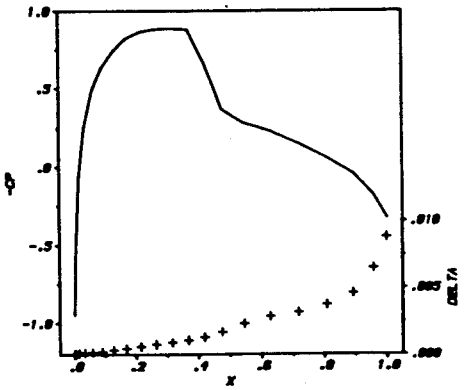

Fig. 4(a)

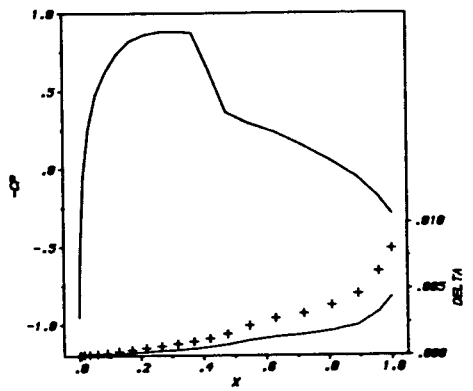

Fig. 4(b) $\omega = 0.5$

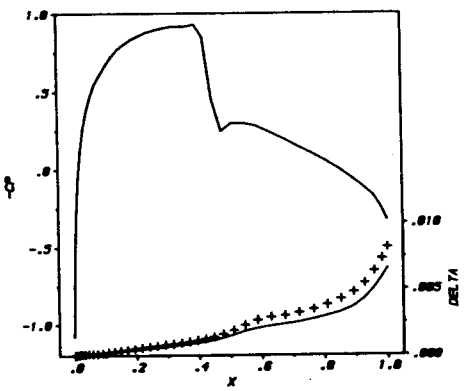

Fig. 4(c) $\omega = 0.6$

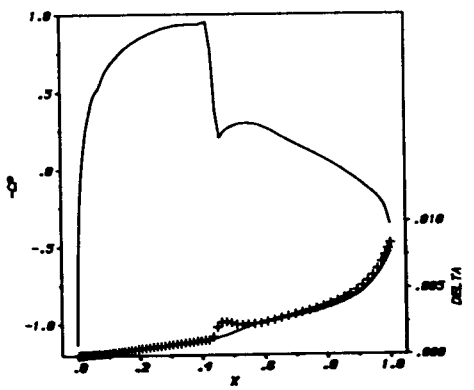

Fig. 4(d) $\omega = 0.7$

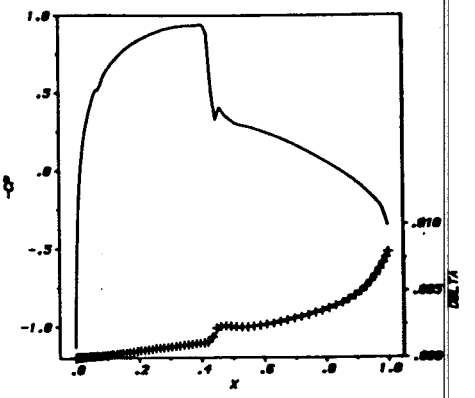

Fig. 4(e) $\omega = 0.8$

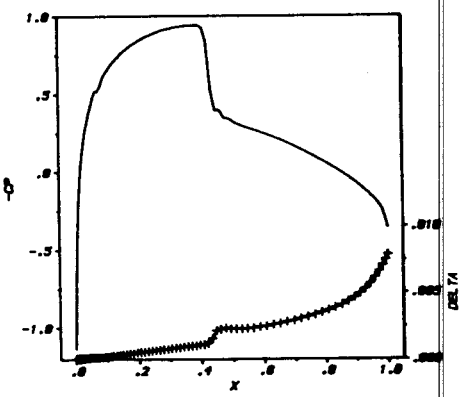

Fig. 4(f) $\omega = 0.9$

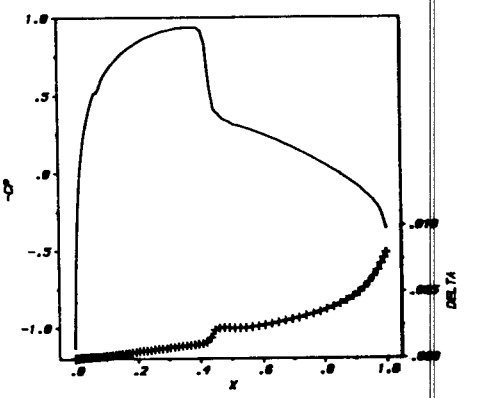

Fig. 4(g) $\omega = 1.0$

Fig. 4 Iterative sequence of pressure coefficient and displacement thickness for NACA 0012 profile (M = 0.77, Re = 4.9 x 10^6, β = 0 deg)

tested by Rechter et al. [14] for a transonic compressor cascade at an inlet Mach number of 0.8. The stator is distinguished by a flow turning angle of 37 deg and a gap-to-chord ratio of 0.83. The design was aimed at a shock-free recompression with attached boundary layer and acceptably low losses in the near off-design range. Figure 6 shows the prescribed design Mach number distribution as a solid line together with some measured values from experimental verification. The authors [14] state that the design conditions with M = 0.8 and an axial velocity density ratio Ω = 1.05 correspond to measurements around M = 0.77 and Ω = 1.09, due to the blockage effects of side wall boundary layers, which are accounted for in different ways in the design process and the experiment. While the discrepancies at the leading edge are due to limitations of Schmidt's design method [15] the disagreement at about 40 percent of chord length was attributed to a laminar separation bubble.

Our analysis is based on Ω = 1 and the profile data given except for the leading edge region, which was rather coarsely

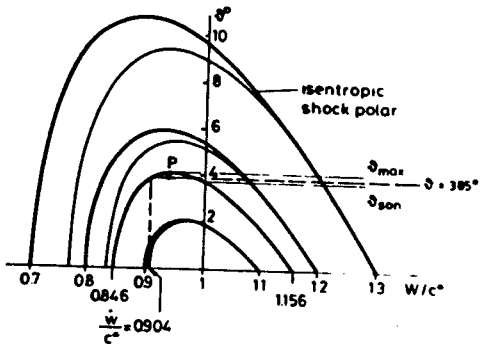

Fig. 5 Velocity deflection angle across shock

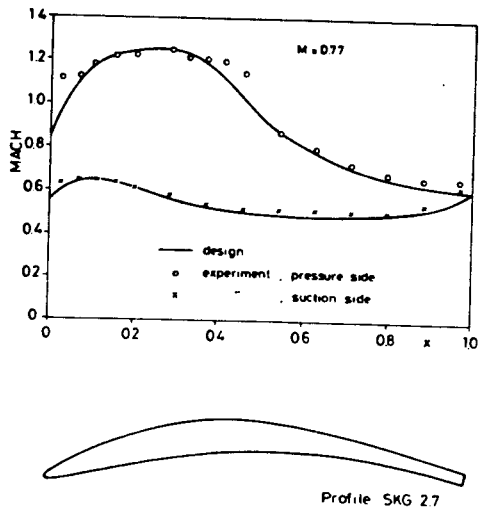

Fig. 6 Prescribed and measured Mach number variation for the SKG 2.7 cascade ([14]: $g/c = 0.821$; $\beta_s = 103.6$ deg; $\beta_1 = 126.7$ deg; $\beta_2 = 90.0$ deg)

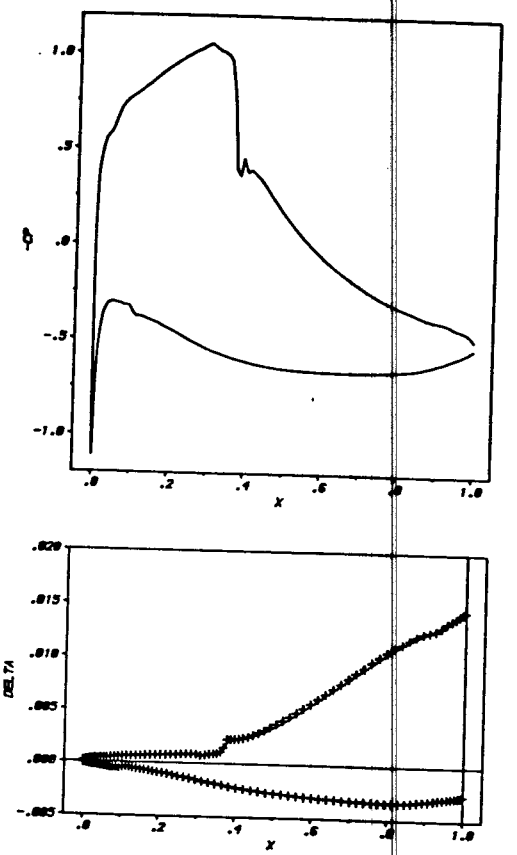

Fig. 7 Analysis of SKG 2.7 cascade at M = 0.8

displayed and needed some modifications. Letting transition take place near laminar separation we encounterd shock-induced transition. As the treatment of shock-transitional boundary layer interaction is beyond the capabilities of our code we specified (with reference to [14]) transition at 30 percent of the chord length. The following results were obtained for $Re = 1.2 \times 10^6$ and $\omega = 0.5$.

At $M = 0.8$ we encounter a distinct shock impinging on the turbulent boundary layer at $x = 0.36$ (Fig. 7). The shock being again oblique leads to a downstream Mach number just below 1. A further modest increase of inflow Mach number from 0.80 to 0.81 instantaneously caused turbulent boundary layer separation.

It would certainly be unsatisfactory for the practicing engineer to stop at this stage of analysis. Fortunately we can switch over to the design option of the code and apply a semi-inverse solution procedure to the inviscid flow field calculation making use of Sobieczky's fictitious gas concept.

As explained in greater detail in [8, 9] we slightly modify the profile section on the suction surface and perform a fully elliptic potential flow field calculation. The ellipticity of the governing equation is guaranteed by the use of a fictitious gas density–velocity relation, whenever the flow becomes locally supercritical. In extension to the earlier cited publications viscous effects in the design mode are now accounted for by applying the same global iteration procedure as described before for the analysis mode, the only difference being that the pressure coefficient as input variable for the boundary layer calculation is obtained from the fictitious gas analysis result. This approximation leads to an efficient redesign procedure and proves to be appropriate because of the similarity between the isentropic and fictitious gas pressure distributions.

As a consequence of the absence of shocks, the potential flow calculation, which takes most of the overall iteration time, is considerably accelerated. To further speed up the convergence rate, in the design mode the displacement thickness is not only underrelaxed but also locally smoothed, where the rate of smoothing is proportional to the local deviation in displacement thickness between two successive global iterations. Thus smoothing will be reduced while approaching the converged solution.

When convergence of the inviscid/viscous iteration loop is achieved, the initial value problem inside the supersonic bubble is solved by a second-order accurate method of characteristics using now the isentropic gas density–velocity relation. The integration begins at the sonic line and arrives at the new part of the effective airfoil contour which is determined by the condition of its constant value of the stream function. Figure 8 shows the supersonic bubble and the corresponding isentropic gas pressure distribution obtained by the method of characteristics. It should be noted that in striving for an improvement of the blade's performance the chosen example presents a fairly tough test case, because the efficiency of the original design is already not too bad. In carrying out the inverse redesign procedure we encountered a sensitive equilibrium between the avoidance of expansion peaks near the nose and compression shocks terminating the supersonic zone. This may be seen directly from the concentration of characteristic lines in these regions (Fig. 8) and an indentation of the pressure distribution and the sonic line (Fig. 9). This time the finite area method with first-order artificial viscosity was used to calculate the flow through the redesigned cascade with the displacement thickness being added to the profile. This balancing problem is further enhanced by the fact that the flow in the recompression zone over the original blade is already very near to separation. Thus several constraints are

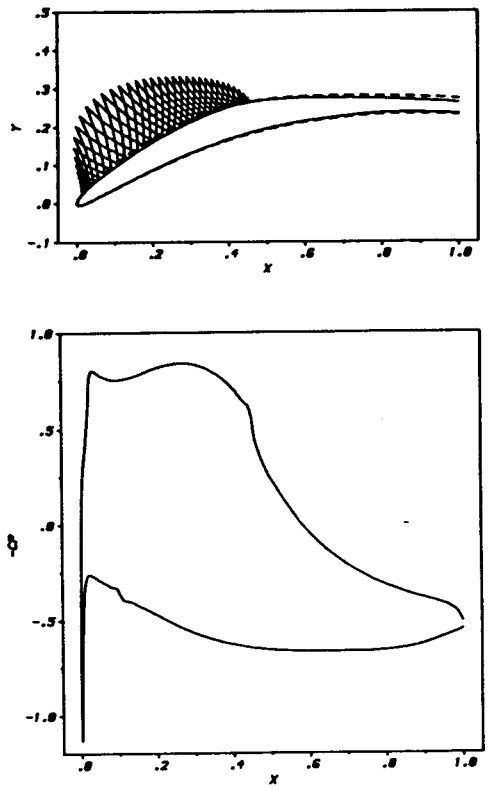

Fig. 8 Redesigned cascade at M = 0.8: supersonic bubble and pressure distribution

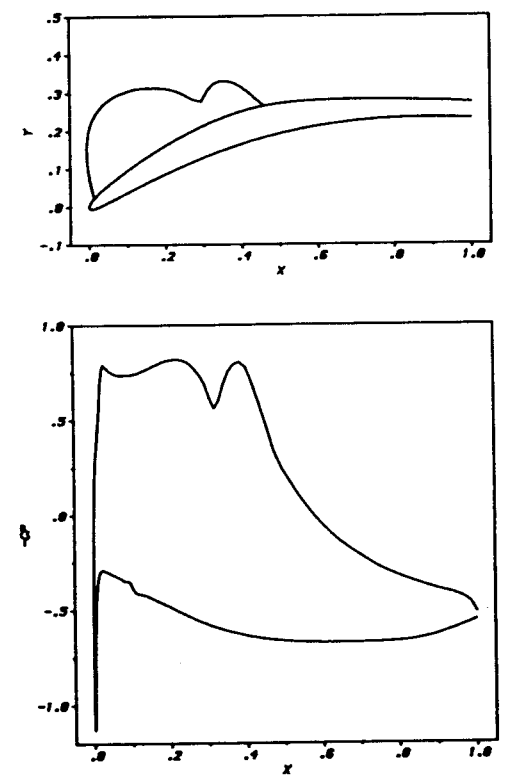

Fig. 9 Analysis of outer inviscid flow around redesigned cascade including displacement thickness at M = 0.8

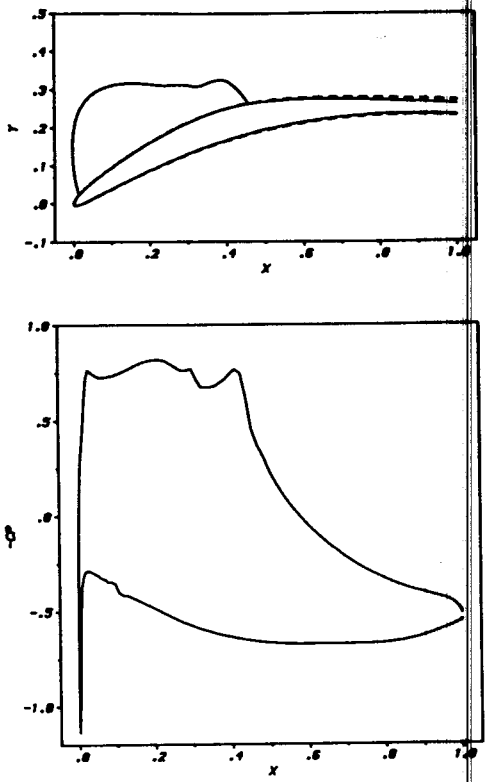

Fig. 10 Complete verification analysis of redesigned cascade at M = 0.8

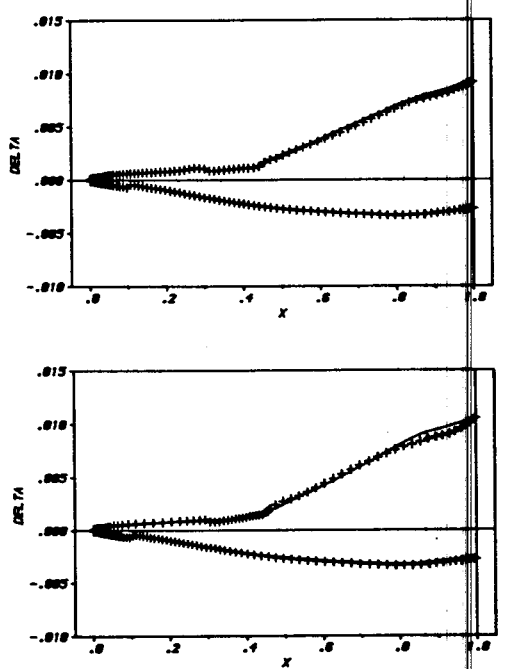

Fig. 11 Comparison of displacement thickness resulting from: (a) analysis (upper figure); (b) redesign (lower figure) at M = 0.8

narrowing down the margin of appropriate contour modifications.

Subtraction of displacement thickness from the effective contour yields the new bare blade shape. The supersonic part of the effective airfoil obtained by the method of characteristics in connection with streamline integration is already smooth. Thus, to avoid slope discontinuities in the new profile contour, we locally smooth the displacement thickness variation over the transition region before subtraction in case boundary layer transition had taken place in the supersonic zone.

To verify the improvements of our redesign we repeat the complete inviscid/viscous flow analysis and in fact recover a

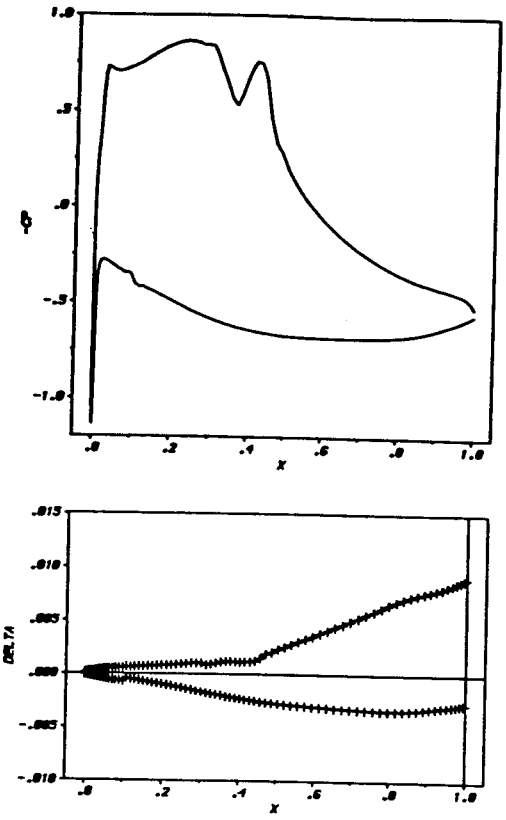

Fig. 12 Analysis of redesigned cascade at M = 0.81

shock-free solution (Fig. 10). As no smoothing technique was applied in the analysis mode the preshock wiggles in the pressure distribution may not only originate from the abovementioned indentation but also from the interaction with the supersonic part of the boundary layer in the course of the iteratively developing solution.

The corresponding displacement thickness is shown in Fig. 11(*a*). There are only small deviations from the displacement thickness obtained by the redesign procedure (Fig. 11*b*). In Fig. 11(*b*) the displacement thickness calculated by the use of the isentropic gas pressure distribution obtained in connection with the method of characteristics (indicated by crosses) is compared to that obtained by the use of the fictitious gas pressure during the last global iteration cycle in the redesign mode (solid line). The smallness of the difference between these two curves in fact confirms the utility of our simplifying approximation for the pressure distribution during iterative redesign; it justifies the use of the fictitious gas pressure as boundary condition for the boundary layer calculation within the supersonic bubble.

Slightly raising the inflow Mach number from 0.8 to 0.81 (Fig. 12) causes again shock losses, but the severe limit of this test case is given by turbulent boundary layer separation, which occurs just beyond M = 0.81.

Conclusion

We have described the extension of an efficient numerical analysis and redesign tool for engineering purposes that takes into account shock–boundary layer interaction for cascades at off-design operating conditions. An easy mapping procedure, a smooth local grid clustering, an analytical solution for the viscous interaction zone, a simple direct coupling and iterative solution technique are the main features of the computational modules contributing to that extension. The flexibility of the code in its analysis and redesign modes has been demonstrated by a user-oriented example calculation. Consideration of quasi-three-dimensional and rotation effects, a more adequate wake modeling, and a refined inviscid shock calculation method belong to further improvements now under development.

References

1 Bohning, R., and Zierep, J., "Der senkrechte Verdichtungsstoss an der gekrümmten Wand," *ZAMP*, Vol. 27, 1976, pp. 225–240.

2 Bohning, R., and Zierep, J., "Normal Shock–Turbulent Boundary Layer Interaction at a Curved Wall," AGARD-CP-291, 17/1–17/8, 1980.

3 Rotta, J. C., "Turbulent Boundary Layer Calculations With the Integral Dissipation Method," *Computation of Turbulent Boundary Layers*, AFOSR-IFP Stanford Conference, Vol. I, 1968, p. 177 (also *Ing. Archiev*, Vol. 38, 1969, pp. 212–222).

4 Dulikravich, D. S., and Sobieczky, H., "Shockless Design and Analysis of Transonic Cascade Shapes," *AIAA Journal*, Vol. 20, No. 11, 1982, pp. 1572–1578.

5 Melnik, R. E., Chow, R., and Mead, H. R., "Theory of Viscous Transonic Flow Over Airfoils at High Reynolds Number," AIAA Paper No. 77-680, 1977.

6 Lekoudis, S. G., and Inger, G. R., "Computation of the Viscous Transonic Flow Around Airfoils With Trailing Edge Effects and Proper Treatment of the Shock/Boundary Layer Interaction," AIAA Paper No. 82-0989, 1982.

7 Melnik, R. E., and Chow, R., "Asymptotic Theory of Two-Dimensional Trailing Edge Flows," NASA SP 317, 1975.

8 Sobieczky, H., and Dulikravich, D. S., "A Computational Design Method for Transonic Turbomachinery Cascades," ASME Paper No. 82-GT-117, 1982.

9 Dulikravich, D. S., and Sobieczky, H., "Design of Shock-Free Cascades Including Viscous Boundary Layer Effects," ASME Paper No. 83-GT-134, 1983.

10 Dulikravich, D. S., "Fast Grid Generation of Three-Dimensional Computational Boundary – Conforming Periodic Grids of C-type," NASA/AFOSR Symposium on Numerical Generation of Curvilinear Coordinate System and Use in the Numerical Solution of Partial Differential Equations, Nashville, TN, Apr. 13–16, 1982.

11 Hobbs, D. E., Wagner, J. H., Dannenhoffer, J. F., and Dring, R. P., "Experimental Investigation of Compressor Cascade Wakes," ASME Paper No. 82-GT-299, 1982.

12 Sobieczky, H., and Stanewsky, E., "The Design of Transonic Airfoils Under Consideration of Shock Wave Boundary Layer Interaction," ICAS Paper No. 76-14; DFVLR Report IB 251-76 A 26, 1976.

13 Jou, W. H., and Murmann, E. M., "A Phemomenological Model for Displacement Thickness Effects of Transonic Shock Wave–Boundary Layer Interactions," AGARD-CP-291, 15/1–15/9, 1981.

14 Rechter, H., Schimming, P., and Starken, H., "Design and Testing of Two Supercritical Compressor Cascades," ASME Paper No. 79-GT-11, 1979.

15 Schmidt, E., "Computation of Supercritical Compressor and Turbine Cascades With a Design Method for Transonic Flows," ASME Paper No. 79-GT-30, 1979.